

Long-lifetime current-driven rotating kink modes in a non-line-tied plasma column with a free end

T. P. Intrator,¹ I. Furno,¹ D. D. Ryutov,² G. Lapenta,³ L. Dorf,¹ and X. Sun¹

Received 30 July 2006; revised 6 December 2006; accepted 4 January 2007; published 12 May 2007.

[1] We show the first experimental evidence for a magnetohydrodynamic kink instability in a current rope with one end that is free to move. This free end is partially insulated by sheath resistivity, so that the usual frozen in flux assumption for magnetohydrodynamics is violated in this region. The free end is therefore not line-tied to the axial boundary. We find the instability threshold is well below the classical Kruskal-Shafranov threshold, culminating in a long-lifetime saturated state. The presence of an axial flow further lowers the kink threshold and gives rise to a doppler-shifted frequency from rotation of the kink, where the eigenfunction is axially pushed in the flow direction. This lowered threshold may give rise to kink instabilities in situations with small magnetic twist that would otherwise be considered stable. Striking agreement with a theoretical analysis is demonstrated. The existence of a free end may be important for open flux tubes attached to the Sun, galactic jets associated with accretion discs, and spheromak startup.

Citation: Intrator, T. P., I. Furno, D. D. Ryutov, G. Lapenta, L. Dorf, and X. Sun (2007), Long-lifetime current-driven rotating kink modes in a non-line-tied plasma column with a free end, *J. Geophys. Res.*, *112*, A05S90, doi:10.1029/2006JA011995.

1. Introduction

[2] Many basic properties of the magnetic field can be deduced by considering the long thin flux tube. These current or magnetic flux ropes contain embedded magnetic flux and current, with diameter smaller than both the radius of curvature of the field lines and the tube scale length. Flux ropes are the building blocks of magnetic configurations and have applications to space, astrophysical, and fusion plasmas. Magnetic forces distort these current ropes in three dimensions, for instance via the kink instability. The current-driven kink instability is a magnetohydrodynamic (MHD) instability which affects current carrying plasmas in natural and laboratory settings. Here we show experimental data demonstrating that a free end boundary condition and flow along the flux rope can substantially reduce the kink stability threshold and induce rotation of the current channel [Furno *et al.*, 2006]. These effects may be important during the relaxation of current carrying plasma structures in the solar heliosphere, astrophysical jets, and magnetosphere. Other applications may include spheromak startup and plasma spacecraft thrusters.

1.1. Kinked Flux Ropes in Nature

[3] Sakurai [1976] was the first to identify kinked flux rope dynamics with solar filament eruptions. Recent obser-

vational measurements [Rust and LaBonte, 2005] have been used to demonstrate that the MHD kink instability occurs in solar flux ropes which can disrupt yielding twisted magnetic clouds [Kumar and Rust, 1996] that thread the solar system. Much of the solar magnetic flux which has one end anchored to the Sun opens up into interplanetary space. For example, coronal holes source the fast solar wind [Schrijver and Cornelis, 2000]. Bulk plasma flows are important as well and are often observed in coronal loops [Krall and Chen, 2005] as well as the solar wind itself. The kink instability is important for MHD models of astrophysical jets [Lovelace, 1976; Li *et al.*, 2001] and is often invoked to explain the observation of kinked structures with synchrotron emission [Benford, 1997]. One end of these jets appears bound to the galactic accretion disc, but the length of the jet can very long, i.e., many Alfvén wave travel times. During this time interval, particles at the free end can be decorrelated and isolated by particle collisions from particles at the bound end.

1.2. Kinked Flux Ropes in the Laboratory

[4] In laboratory plasmas, kink modes are observed in applied field magnetoplasma thrusters where a correlation has been established between the kink instability and performance deterioration at high current [Zuin *et al.*, 2004]. MHD kink modes have been observed in laboratory Z-pinch [Verhage *et al.*, 1978] and tokamak plasmas. During spheromak formation, kinks of finite length flux ropes [Sovinec *et al.*, 2001] are thought to mediate the conversion of toroidal to poloidal magnetic flux [Hsu and Bellan, 2003].

1.3. Kruskal-Shafranov Description of the Kink

[5] Since the current driven kink is ubiquitous, great effort has been devoted to derive the mode structure and instability threshold. Kruskal [Kruskal and Tuck, 1958] and

¹Plasma Physics, Los Alamos National Laboratory, Los Alamos, New Mexico, USA.

²Lawrence Livermore National Laboratory, Livermore, California, USA.

³Plasma Theory, Los Alamos National Laboratory, Los Alamos, New Mexico, USA.

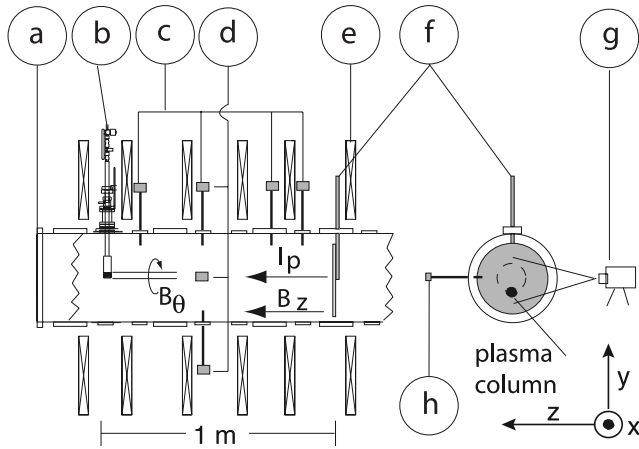


Figure 1. Experimental configuration with diagnostics and coordinate system. Shown are (a) a portion of the 4 m long \times 0.2 m radius vacuum vessel, (b) plasma gun, magnetic probes in (c) an axial array and (d) an azimuthal array, (e) magnet coils imposing a B_z parallel to the current I_p , (f) external anode. On the right, an axial cut of the device close to the external anode shows (g) the viewing geometry of the fast CCD camera and (h) the bidimensional magnetic probe that measures $(\delta B_x, \delta B_y)$ at the edge. Schematically indicated here and with the same geometry in Figure 5 is the plasma column whose end gyrates at the external anode.

Shafranov [Shafranov, 1956] considered first the ideal MHD stability of a cylindrical plasma column with magnetic field components $(0, B_\theta, B_z)$ using cylindrical coordinates (r, θ, z) . For an infinitely long (equivalent to axially periodic) column, they found linearly unstable helical kink perturbations $\xi = e^{i(m\theta + k_z z)}$ with $|k_z| = 2\pi/L$, $|m| = 1$ and $k_z \cdot m < 0$ when the plasma current I_p exceeds the Kruskal-Shafranov limit

$$\begin{aligned} \mu_0 I_{KS} &= 4\pi^2 a^2 B_z / L \\ &= 2k_0 \pi a^2 B_z \end{aligned} \quad (1)$$

where a and L are the radius and length of the current channel, respectively, and ξ is the displacement of the plasma column from the equilibrium position. The wave number

$$k_0 = B_\theta / (a B_z)|_{r=a} \quad (2)$$

is expressed in terms of the magnetic fields and their twist at the edge. The K-S analysis leads to the conclusion that the wave number k_{KS} has the value $k_0 = \mu_0 I_p / (2\pi a^2 B_z)$. The K-S theory has been quite successful in predicting the behavior of toroidal plasmas with periodic boundary conditions. The major result of this paper is the experimental conclusion that with different axial boundary conditions and flow, kink instability can occur with substantially less twist than given by $k_0 = k_{KS}$.

1.4. Deviations From the Kruskal-Shafranov Description

[6] In finite-length linear systems, substantial deviations from K-S predictions are expected because the different axial boundary conditions [Ryutov *et al.*, 2004, 2006;

Lanskii and Shchetnikov, 1990; Hegna, 2004] change the force balance and give rise to different eigenfunctions. Nevertheless, K-S results are recovered if there exists a radially distant conducting boundary at $r = b$ along with perfectly line-tied (PLT) ends that constrain the plasma to be stationary, i.e., $\xi|_{z=0} = \xi|_{z=L} = 0$. The distant radial boundary presumption is equivalent to assuming that the return current radius b is far away from the flux rope radius $a \ll b$. Agreement with K-S predictions has been reported for laboratory devices, where PLT was attributed to the presence of highly conducting end plates [Bergerson *et al.*, 2006], and in open systems to a local discontinuity on the Alfvén velocity that forms a virtual boundary [Hsu and Bellan, 2003; Zuin *et al.*, 2004].

[7] It has been theoretically demonstrated that sufficiently large plasma sheath resistance permits one end to be “free,” and therefore the PLT condition must be replaced by one that allows for finite plasma column displacements [Ryutov *et al.*, 2006]. The importance of the displacement and sheath resistance in plasma stability has long been recognized [Kadomtsev, 1966; Berk *et al.*, 1990; Zweibel and Boozer, 1985]. Partially non-line-tied or “free end” boundary conditions along with axial plasma flow can modify both the threshold for the onset of the kink instability and mode structure [Ryutov *et al.*, 2006]. New predictions include (1) a kink threshold below half the K-S limit, (2) a rotation of the kink with specific parity, and (3) axial mode “skewness” convected by axial plasma flow.

[8] We describe the first direct experimental evidence of a current driven rotating kink mode where the stability and mode structure are strongly affected by the partially line-tied “free” end [Furno *et al.*, 2006]. All the above theoretical predictions are verified.

2. Experimental Realization

[9] This is an experimental study of the kink mode using a linear screw pinch generated with an electrostatic plasma gun [Fiksel *et al.*, 1996]. The Reconnection Scaling Experiment (RSX) [Furno *et al.*, 2003] was used to verify recent theoretical predictions of Ryutov *et al.* [2006].

2.1. Formation of the Screw Pinch

[10] The experimental apparatus is sketched in Figure 1 which shows the experimental setup. There is a view of the plasma gun located at $z = 0$ which is radially inserted into the center of the RSX cylindrical vacuum vessel (4 m length \times 0.2 m radius). A miniature hydrogen arc plasma source inside the plasma gun located at one end of a vacuum vessel generates a current stream. This forms a cylindrical column in the externally imposed constant, uniform, axial magnetic field of $B_z = 120$ Gauss (Figure 1e). A screw pinch is formed by driving a current in the plasma when the gun anode is negatively biased with respect to an external anode (50×10^{-4} m² stainless steel plate) which is electrically isolated from the vacuum vessel. The external anode can be positioned at different axial locations $-3 \text{ m} < z < -0.3 \text{ m}$ so that the length L of the screw pinch can be varied.

2.2. Plasma Profiles

[11] Electron density n_e , temperature T_e , and pressure $p_e = n_e \times T_e$ are simultaneously measured using a movable triple

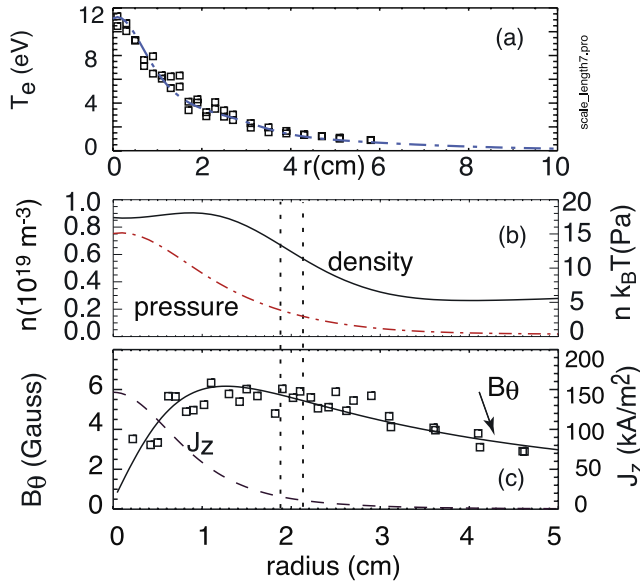


Figure 2. Radial profiles of (a) electron temperature, (b) density and pressure, and (c) azimuthal magnetic field data (squares) with analytic fit (solid) and axial current density $J_z(r)$ (dashed). Vertical dotted lines indicate the error bounded estimate of a from equations (20) and (21).

electrostatic probe with a 1 mm tip separation. The profiles of electron density were modeled with a Gaussian dependence $n_e(r) = c_0 \exp \{ -[(r - r_0)/(\sqrt{2}\sigma_n)]^2 \}$ and an added linear offset $c_1 r + c_2$ to account for a density halo outside the column. The column radius is r , with radial offset $r_0 \approx 0.76 \times 10^{-2}$ m, an edge density scale width is $\sigma_n \approx 1.0 \times 10^{-2}$ m, the Gaussian amplitude is $c_0 \approx 0.53 \times 10^{19} \text{ m}^{-3}$ and for the linear offset function the slope is $c_1 \approx -4.2 \times 10^{19} \text{ m}^{-3}/\text{m}$ with y intercept $c_2 \approx 0.42 \times 10^{19} \text{ m}^{-3}$.

[12] The temperature profiles are modeled using Bennett pinch shape $T_e(r) = T_{e0} [1 + ((r - r_0)/\sigma_T)^2]^{-2}$, where $T_{e0} \approx 12 \text{ eV}$, r , and $r_0 \approx 0$ are the central temperature, radius, and radial offset, respectively, and σ_T is a scale width. The scale radial width for Bennett pinch T_e fit is $\sigma_T \approx 0.02\text{--}0.03$ m. Central electron density and temperature are $n_{e0} = 1 - 6 \times 10^{19} \text{ m}^{-3}$ and $T_{e0} = 5 - 14 \text{ eV}$, and axially decrease away from the gun. The axial flow speed $v_z \approx 5 \times 10^4 \text{ m/s}$ has been estimated using a quasi one-dimensional MHD axial flow model that neglects $J \times B$ forces (see section 6.2).

[13] Radial profiles for plasma quantities of interest are shown in Figure 2. The electron temperature T_e was measured with a triple probe, and the error bars (estimated to be $\pm 10\%$ at the edge) increase near the periphery at lower temperature and density. The density n and electron pressure $p = nk_B T_e$ are shown in Figure 2b. Magnetic measurements of B_x and B_y in the $x - y$ cut plane allow calculation of axial current $J_z = \nabla \times (B_x \hat{x} + B_y \hat{y})/\mu_0$ and the field line twist. These are displayed on Figure 2c.

[14] We will characterize the external kink mode in terms of the current and radially averaged density inside some column radius and the axial magnetic field outside that radius. Later in section 6.1 we will conclude that the exterior of the current distribution is near $r \approx 0.02$ m.

The Alfvén speed $v_{A0} = B_{z0}/(\mu_0 n m_i)^{1/2}$ defined in terms of the background axial magnetic field and the peak density at the column center is approximately $v_{A0} \approx 9 \times 10^4 \text{ m/s}$. To simplify the algebra, an averaged Alfvén speed \bar{v}_A is defined to be $\sqrt{2}$ larger than that computed with an averaged density [Ryutov *et al.*, 2006].

$$\bar{n} = \frac{2}{a^2} \int_0^a n(r) r dr \quad (3)$$

$$\bar{v}_A \equiv \sqrt{2} v_{A0} = \sqrt{2} \frac{B_{z0}}{(\mu_0 m_i \bar{n})^{1/2}} \quad (4)$$

The radius $a \approx 0.02$ m will be chosen later in section 6.1 after invoking constraints from experimental data. We will find that within the experimental error bars, $\bar{n} \approx 0.6 - 0.8 n_0$, where $n_0 = n(r = 0)$ is the density at the column center. Consequently, $\bar{v}_A \approx 1.5 - 1.8 \times v_{A0} \approx 1.4 - 1.7 \times 10^5 \text{ m/s}$.

[15] The time evolution of the plasma current measured at the external anode is shown in Figure 3a. The plasma current begins at $t = 0$ when the bias is turned on (arc discharge starts at $t = -1$ ms) and after $\approx 150 \mu\text{s}$ reaches a flat top phase whose duration can be adjusted between $\approx 1 - 10$ ms. The total plasma current $I_p = 0.1 - 1 \text{ kA}$ during the flat top phase is determined by the bias voltage and additional resistance inserted in the circuit and increases at $dI_p/dt = 20 \text{ Amp}/\mu\text{s}$.

3. Magnetic Characterization of the Kinking Flux Rope

3.1. Long-Lifetime Unstable States

[16] The MHD activity is monitored by two arrays of magnetic probes that include a total of seven coils inserted in the vacuum vessel at $r = 0.15$ m to measure the azimuthal magnetic field B_θ . In the axial array (Figure 1c) four

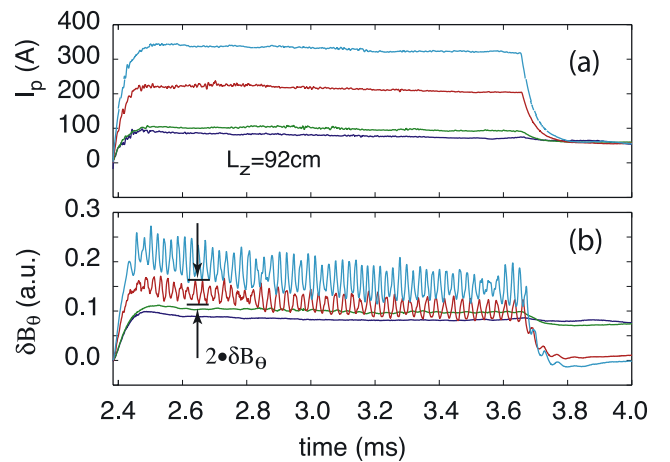


Figure 3. Time histories of (a) plasma current to the external anode and (b) perturbed azimuthal magnetic field δB_θ measured outside the current rope. Time is referenced in msec after arc initiation. The plasma current $I_p(t) \approx 330 \text{ A}$ to the external anode is the same as the example chosen for display in Figure 4a.

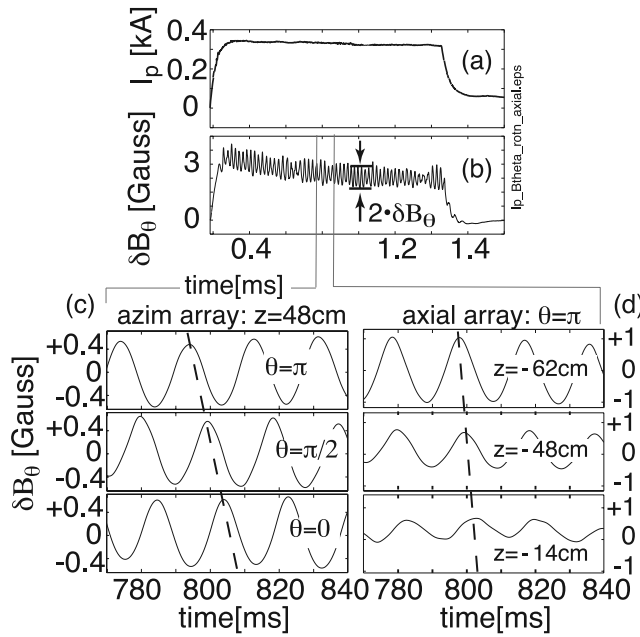


Figure 4. Time histories of (a) the plasma current I_p to the external anode, (b) perturbed azimuthal magnetic field δB_θ measured outside the current rope, time referenced in msec after arc initiation. B_θ , from the (c) azimuthal and (d) axial arrays of magnetic probes during the flat top phase of the plasma current ($I_p = 300$ A), time referenced to the bias voltage start. Probes were positioned at $r = 0.15$ m, plasma column length is $L = 0.92$ m, \hat{x} , \hat{y} , \hat{z} , and B_z as in Figures 1 and 5. Note that $k_z > 0$ and $m = -1$.

magnetic probes are positioned at $\theta = 90^\circ$ (top of the vessel) and axially located at $z = -0.14, -0.48, -0.62, -0.76$ m. In the azimuthal array (Figure 1d) the four magnetic probes are located at $z = -0.48$ m and equispaced by $\pi/2$ in the azimuthal direction. One magnetic probe is shared by the two arrays, and signals are passively integrated before digitizing at 20 MHz.

[17] Time histories of plasma current I_p from a series of shots with one choice of column length $L_z = 0.92$ m with successively increasing plasma current I_p are shown in Figure 3a. The plasma current is constant in time for each shot and ranges from $I_p = 60$ A which turns out to be below the kink threshold to $I_p = 320$ A which greatly exceeds the experimental stability threshold. The time histories of $B_\theta(t)$ as measured by the magnetic probe located at $z = -0.48$ m, $\theta = \pi/2$ in Figure 3b indicate that for small I_p there are no discernible oscillations in $\delta B_\theta(t)$, whereas for large values of I_p , oscillations are clearly evident. We will define the value δB_θ to be the zero to peak amplitude.

[18] In principle, the growth of any ideal MHD mode occurs on the Alfvén time and is explosively fast. The existence of the long-lifetime state is of interest because some saturation mechanism appears to be dominating the late time evolution of the flux rope external configuration. Aside from noting the existence of this long-lifetime state, we will not in this paper investigate further the saturation mechanisms or causes.

3.2. Kink Propagation

[19] We now choose an example of strongly saturated unstable flux rope data similar to that of Figure 3, where the time history of $I_p(t)$ is shown in Figure 4a. The time evolution of $B_\theta(t)$ as measured by the magnetic probe located at $z = -0.48$ m, $\theta = \pi/2$, is shown in Figure 4b. Sinusoidal oscillations have an $m = -1$ azimuthal periodicity. An expanded time window shows that the plasma rotation has azimuthal phase delay as shown in Figure 4c and axial phase delay as shown in Figure 4d. The dashed lines indicate axial and azimuthal delays corresponding to a helically kinked flux rope that rotates.

[20] The schematic shown in Figure 5 illustrates the three-dimensional (3-D) geometry of the kink, including the same experimental geometry and coordinate system as in Figure 1. The radial displacement at the free end is significant, and the sense of the corkscrew helix is paramagnetic, i.e., right-handed such that the background magnetic field is amplified by the kink.

[21] The rotation of the helix that produces signals such as shown in Figure 4 is observed to be in the ion diamagnetic rotation direction. This rotation appears to “screw” into the external anode. If one tracks a point on the helix at fixed azimuthal angle, it will appear to propagate toward the gun. At fixed axial location, propagation is in the negative $\hat{\theta}$ direction. Note that the distance from the gun is taken to be negative in this coordinate system.

3.3. Extrapolation to Instability Threshold

[22] As seen from Figure 3b, oscillations are undetectable for small currents lower than a current threshold that we define as I_{crit} but become strong when $I_p > I_{crit}$. These oscillations grow on a timescale $\tau \approx 4\mu\text{s}$ which is of the order of the axial Alfvén transit time for the flux rope half length $\tau_A \approx \frac{1}{2}v_{A0}/L_z \approx 4\mu\text{s}$. The average amplitude of the δB_θ oscillations during the flat top phase scales linearly with I_p as summarized in Figure 6 where the plasma current is varied in the range $90 \text{ A} \leq I_p \leq 190 \text{ A}$.

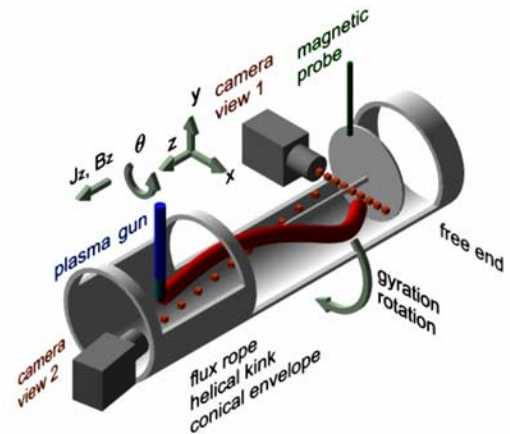


Figure 5. Schematic of the cylindrical experimental geometry. The axially skewed helix envelope rotates azimuthally while axial flow expands it toward the free end. Also shown are the coordinate system, camera view and magnetic probe locations from Figure 9.

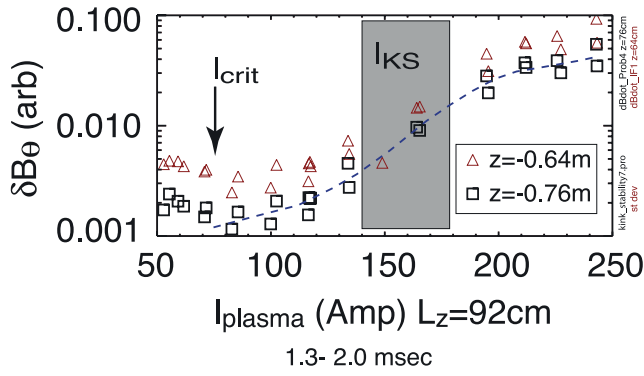


Figure 6. The asymptotic stability threshold I_{crit} can be inferred from data sets similar to Figure 3 where $\delta B_\theta \rightarrow 0$ is plotted as a function of I_p . The determination of I_{KS} is discussed in section 6.1 along with Figure 10.

[23] From measurements of the perturbed azimuthal magnetic field δB_θ data such as shown in Figure 3, one can plot the magnetic disturbance against drive amplitude I_p . The asymptotic value of I_p as the $\delta B_\theta \rightarrow 0$ will then be defined as the kink stability critical current threshold I_{crit} , which for these data is $I_{crit} = 70 \pm 7$ Amp. This method also has the advantage that nonlinear effects which likely come into play at large drive I_p are also vanishingly small in the asymptotic limit. For reference, we also indicate here the Kruskal-Shafranov threshold that will be calculated later in section 6.1.

[24] Figure 7 shows the rotation frequency f_{rotn} as the plasma current $1.3 < I_p/I_{crit} < 2.7$ is varied. The asymptotic rotation frequency f_{rotn} at the stability threshold I_{crit} can be inferred from the same data sets used for Figure 6. For these data f_{rotn} is plotted as a function of I_p . The linear fits of these data (dashed line in Figure 7) are used to infer the rotation frequency $f_{crit} = 27$ kHz at the critical current, $I_p = I_{crit}$, and $L_z = 0.92$ m. This confirms the linear theory predictions [Ryutov *et al.*, 2006].

3.4. Mode Structure

[25] Figure 8 shows magnetic measurements that diagnose the amplitude of the $m = -1$ mode close to critical threshold for $I_p \approx 1.3 \times I_{crit}$. Since a fixed end boundary condition holds at the gun, the large amplitude of the mode at $z = -0.75$ m can only occur if the plasma is not line-tied at the external anode, i.e., $\xi|_{z=L} \neq 0$. Two counterpropagating modes specified by equation (11) can also be rewritten using a phasor representation. This allows use of the usual experimental method of identifying time delay that corresponds to phase delay for the sinusoidal $B_\theta(t)$. We note in passing that the single phasor representation for two waves does not capture the two wave properties but is only a convenient way to establish a time delay. The gyration envelope yields a theoretically predicted amplitude of $B_\theta(t)$ for an external magnetic probe located at $r = 0.15$ m. The amplitude δB_θ is shown by the solid line in Figure 8, with no free parameters. There is excellent agreement between predictions and data.

4. Optical Images

[26] From the magnetic perturbations we have already concluded that one end is free. This result is also confirmed

by fast camera images of the plasma column at the external anode. The viewing geometry is shown in Figure 5. The plasma gun inserts radially as shown in Figure 1, shoots a flux rope axially, and creates a current channel that helically deforms and rotates. Camera view 2 yields a foreshortened perspective view of the flux rope, resulting in images that have been already published in the work of Hemsing *et al.* [2004, 2005]. The other camera view 1 which is used for the Figure 9 data has its view across the diameter of the vacuum vessel very near the external anode. A magnetic probe is located at the same z location, with $\pi/2$ azimuthal separation. The camera labeled “camera view 1” created images of the flux ropes shown in Figure 9, where visible H_α plasma emission is imaged with a Cooke DiCam Pro intensified charge-coupled device (CCD) camera that views the external anode edge, as viewed perpendicular to the z axis.

[27] In Figures 9a and 9b we show two fast gated images per discharge, synchronized with a magnetic probe (see Figure 1). The 200 ns gate time is much shorter than the Alfvén time, and the successive images show respectively the plasma column in the unperturbed equilibrium position and the maximum kinked displacement ξ_L after the onset of the kink instability ($\approx 10 \mu s$ later in time).

[28] For timescales less than the 100–200 μs resistive diffusion time corresponding to the stainless steel external anode thickness, one might presume PLT (perfect line tied) boundary conditions at the external anode. However, the observed sliding of the plasma column over the external anode surface is clearly not consistent with PLT.

5. Theoretical Characterization of a Non-Line-Tied End

5.1. Sheath

[29] Deviations from PLT boundary conditions may appear if the plasma is partially insulated from the external anode by a finite plasma sheath resistance [Ryutov *et al.*, 2006]. In the sheath region, resistivity η_{sh} is substantial compared with smaller plasma resistivity η_p . Even with a perfectly conducting external anode boundary, the plasma side of the sheath can support axial and transverse electric fields. In the sheath region, radial spreading of the axial flux rope current will give rise to a locally increased electric

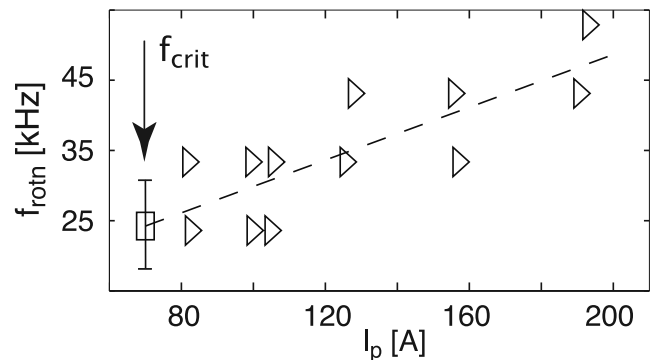


Figure 7. The asymptotic rotation frequency f_{rotn} at the stability threshold I_{crit} can be inferred from the same data sets used for Figure 6. For these data f_{rotn} is plotted as a function of I_p , and $f_{crit} = \lim_{I_p \rightarrow I_{crit}} f_{rotn}$.

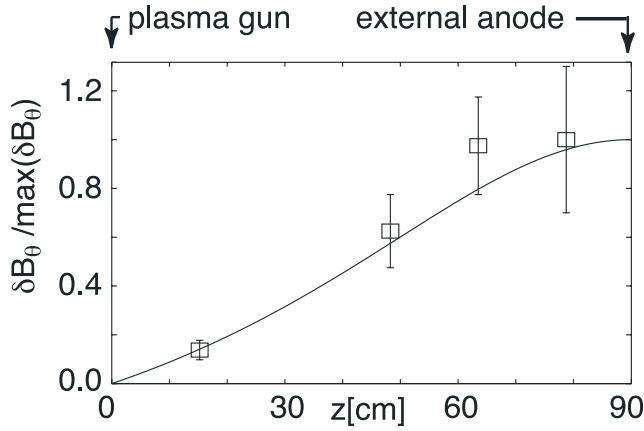


Figure 8. Magnetic evidence for axial mode structure where $I/I_{crit} \approx 1.3$. The δB_θ perturbations increase at the free end as the column near the external anode approaches the magnetic probe. The solid line indicates the theoretical predictions from the eigenfunction equations (11) and (12) with no free parameters.

fields along with decreased axial current density consistent with the relation $\eta_{sh} = E_{sh}/J_{sh}$. If η_{sh} is sufficiently large, the ideal MHD frozen flux assumption fails, i.e., the plasma and magnetic field lines will no longer be constrained to move in unison. Consequently the line-tied or zero displacement boundary condition must be replaced with a more general mixed boundary condition constraint [Ryutov *et al.*, 2006] such as equation (6).

[30] The dimensionless ratio κ of the Alfvén transit time to inductive decay time of the current can be used to characterize the partial insulation $\eta_{sh} \gg \eta_p$. For the present RSX experiments $\kappa \gg 1$ and the MHD frozen flux assumption breaks down in the sheath between plasma and the conducting boundary. We will refer to this condition as perfect non-line-tying (PNLT) boundary condition. Typical plasma parameters include ($a \approx 0.02$ m, $T_e \approx 10$ eV, $n_e \approx 10^{19}$ m $^{-3}$, $v_z/c_s \approx 1$). We estimate $\kappa \approx 15$ from equation (49) in the work of Ryutov *et al.* [2006]

$$\kappa \approx \frac{c_s}{v_z} \left(\frac{c}{a\omega_{pi}} \right)^2 \beta_e^{1/2} \quad (5)$$

where $c_s = (T_e/m_i)^{1/2} \approx 3 \times 10^4$ m/s, $\beta_e = n_e T_e / (B_z^2 / 2\mu_0) \approx 0.25$, $\omega_{pi} = 2\pi f_{pi}$, and $f_{pi} \approx 650$ MHz is the ion plasma frequency.

5.2. Axial Boundary Conditions

[31] The finite-length PNLT boundary condition [Ryutov *et al.*, 2006, 2004] can be formulated as

$$\begin{aligned} \zeta|_{z=0} &= 0 \\ \left(\frac{\partial \zeta}{\partial z} + i \frac{k_0}{2} \zeta \right) \Big|_{z=L} &= 0 \end{aligned} \quad (6)$$

with a complex phasor displacement

$$\zeta(z, t) = \xi_x(z, t) + i\xi_y(z, t) \quad (7)$$

that can be expressed in a Cartesian coordinate system (see Figure 1). We will refer in the following to equation (6) as the perfect non-line-tying (PNLT) condition.

5.3. Magnetic Perturbations

[32] For a thin plasma column approximation ($a \ll r_{wall}, L$) the magnetic field perturbation $\delta B_\theta = (\delta B_x^2 + \delta B_y^2)^{1/2}$ resulting from a spatial perturbation ξ about a location outside the plasma at distance Δr from the equilibrium position is

$$\delta B_0 = -\mu_0 I_p \xi / (2\pi \Delta r^2). \quad (8)$$

[33] For the PNLT condition, a correction to the Cartesian components ($\delta B_x, \delta B_y$) of the magnetic field perturbation outside the plasma at a distance Δr from the equilibrium position can be expressed as

$$\begin{aligned} \delta B_{x,y} &= \pm(3/4)\delta B_0 \\ &= \pm(3/4)B_z k_0 a^2 \xi_L / \Delta r^2 \end{aligned} \quad (9)$$

where the factor of 3/4 follows from the PNLT equation (6).

[34] Near (i.e., 0.01 m axially in front of) the external anode, we use magnetic measurements combined with plasma column images to test equation (9). Gated images such as those in Figures 9a and 9b determine the maximum displacement $y_{d,max}$ and equilibrium y_{eq} positions of emissivity along a sight line parallel to the external anode surface and spaced axially 0.01 m from it.

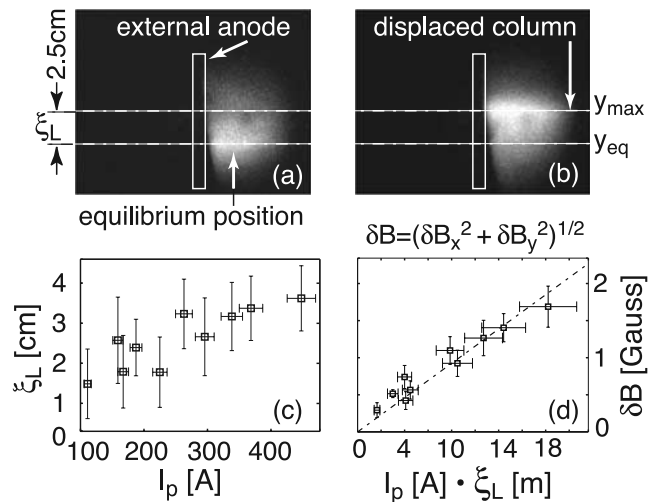


Figure 9. Measurements at the external anode demonstrating a perfectly non-line-tied plasma column. As the plasma gun shoots from right to left, a camera located at view 1 from Figure 5 fast gated (340 ns) image of visible emission near the external anode shows (a) equilibrium and (b) the displaced position ξ_y of the current channel during the rotation. (c) Measured optical displacements ξ_y near the external anode for different plasma current I_p . (d) Magnetic field perturbation $\delta B = (\delta B_x^2 + \delta B_y^2)^{1/2}$ outside the plasma plotted against $I_p \xi_L$ compared with equation (9) (dashed line).

[35] For a series of shots that scan plasma current $100A \leq I_p < 500A$, maximum displacement and the equilibrium position y_{eq} of maximum emissivity $\xi = |y_{d,max} - y_{eq}|$ is shown in Figure 9c. For the same experimental configuration, magnetic perturbations in Figure 9d (δB_x , δB_y) outside the plasma column are measured using a two-dimensional magnetic probe positioned at location $\Delta r = 0.20$ m. Figure 9d shows good agreement with the PNLT predicted scaling in equation (9). Note the direct overlay does not invoke any free parameters to fit the data.

[36] The similarity between optical and magnetic measurements of column displacement and the theoretical predictions for PNLT boundary conditions compels us to conclude that this flux rope is in fact non-line-tied at one end. We believe that in this set of experiments, finite plasma sheath resistance at the external anode breaks the MHD assumption that magnetic flux is frozen into the fluid frame.

5.4. Effects of Flow

[37] One can include parallel plasma flow in this picture of the kink, which modifies the eigen-equation. The switch between laboratory and plasma frame using the Galilean transformation is equivalent to replacing an operator D/Dt by an operator

$$D/Dt \rightarrow \partial/\partial t + v_z \partial/\partial z \quad (10)$$

For both PLT and PNLT end conditions with plasma flow at axial velocity v_z , the most unstable mode (see derivation in equation (9) of Ryutov *et al.* [2006]) can be represented using complex displacement $\zeta(r,t)$ from equation (7) so that

$$\zeta = C(e^{ik_1 z} - e^{ik_2 z})e^{im\theta - i\omega t} \quad (11)$$

where the two axial wave numbers are

$$k_{1,2} = \pm \frac{k_0}{2} \left[(1 - M^2)^{1/2} \mp 1 \right] \quad (12)$$

Here the Mach number is referenced to the averaged Alfvén speed \bar{v}_A defined by equation (4) [Ryutov *et al.*, 2006]. This average Alfvén speed and a Mach number $M = v_z/\bar{v}_A$ will be used in the following comparisons with theory and in section 5.4.

[38] Application of PNLT boundary conditions from equations (6) to the displacement in equation (11), and $k_{1,2}$ from equation (12), one finds the constraint

$$\exp[i(k_1 - k_2)L] = \frac{2k_2 + k_0}{2k_1 + k_0} \quad (13)$$

where we will find k_0 below. When the boundary conditions are accounted for, the PLT constraint requires that

$$k_2 - k_1 = +1 = -2\pi n/L; \quad PLT \quad (14)$$

for integer mode number n , whereas the PNLT constraint requires that

$$k_2 - k_1 = -1 = -\pi n/L; \quad PNLT \quad (15)$$

for odd integer n , and we consider the lowest modes $|n| = 1$. The instability threshold occurs for PLT at values of

$$|k_0| \geq \frac{2\pi|n|}{L} (1 - M^2)^{1/2} \quad (PLT) \quad (16)$$

and for PNLT at values of

$$|k_0| \geq \frac{\pi|n|}{L} (1 - M^2)^{1/2} \quad (PNLT) \quad (17)$$

The PNLT wave numbers for the RSX experiment are then given by equation (12). Note that for zero flow, or $M = 0$ in the lowest mode, the predicted

$$k_{1,2} = 0, \pi/L \quad (18)$$

recovers the finite-length, free-end prediction for k_2 . Experimentally, one measures the amplitude and phase of equation (11) with a single phasor representation for the sum of two phasors, as seen in Figure 8.

[39] For the Kruskal-Shafranov formulation, the critical current for the linear onset of the kink instability can be written either as equation (1) or in terms of axial flux $\Phi_z = \pi r^2 B_{z0}$ to facilitate comparison with our experiment

$$I_{KS} \geq 4\pi\Phi_z/(\mu_0 L_z) \quad (19)$$

This applies to the case of toroidal periodicity. The K-S wave number which is invoked in the standard kink stability derivation is given by equation (2). For the case of a free end the stability threshold turns out to be less than the K-S example. That is, for PNLT $|k_0| \leq k_{KS}/2$ where $k_{KS} = 2\pi/L$, and where k_{KS} corresponds to the critical current I_{KS} as written in equations (1) and (19). For a free end with zero flow, the critical current is half of I_{KS} .

$$\begin{aligned} I_{crit} &= \frac{I_{KS}}{2} (1 - M^2)^{1/2} \\ &= \frac{(2\pi)^2 a^2 B_z}{\mu_0 L} (1 - M^2)^{1/2} \end{aligned} \quad (20)$$

When the flow is significant, the instability threshold can be substantially less than $I_{KS}/2$. The eigenfunctions contain the sum of two components that include a wave number k_0 that is half k_{KS} . Nevertheless, the eigenfunction amplitude for the fixed-end PLT case resembles a one half wavelength shape, and the free-end PNLT case resembles a one quarter wavelength shape.

[40] One can rewrite any of these equations in terms of either I_{KS} or k_0 because $I_{crit}/I_{KS} = k_0/(2\pi/L)$. The wave number and current at the instability threshold are summarized in Table 1, from analytic expressions given by Ryutov *et al.* [2006].

[41] Even at the stability threshold, the helically kinked plasma column rotates with a Doppler-shifted (nonzero) frequency from a convective derivative $D/Dt = \partial/\partial t + v \cdot \nabla \rightarrow -i(\omega - kv)$. Note that for the determination of critical frequency $Re(\omega)$, there is a missing factor of 1/2 that is a typographical error in equation (71) of Ryutov *et al.* [2006]

Table 1. Wave Number and Critical Current for Several Axial Boundary Conditions^a

Ends	k_1/k_{KS}	k_2/k_{KS}	I_{crit}	k_0/k_{KS}
Toroidal	1	0	I_{KS}	1
Periodic	1	0	I_{KS}	1
Fixed	0	-1	I_{KS}	1
Fix + flow	$(A_M - 1)$	$-(A_M + 1)$	I_{KS}/A_M	1
Free	0	-1/2	$I_{KS}/2$	1/2
Free + flow	$\frac{1}{2}(A_M - 1)$	$-\frac{1}{2}(A_M + 1)$	$I_{KS}/(2A_M)$	1/2

^aWe define $I_{KS} = (2\pi)^2 a^2 B_z / (\mu_0 L)$ and $k_{KS} = 2\pi/L$ for the $n = 1$ mode and $A_M = (1 - M^2)^{-1/2}$.

and equation (4) of Furno *et al.* [2006]. The threshold frequency is

$$\begin{aligned} Re(\omega) &= -\frac{\pi v_z}{2L} (1 - M^2)^{1/2} \\ &= -\frac{\pi \bar{v}_A}{\sqrt{2}L} M (1 - M^2)^{1/2} \end{aligned} \quad (21)$$

where M is an Alfvén Mach number, $M \equiv v_z/\bar{v}_A$, $|M| < 1$. For the coordinate system of Figures 1 and 5, $v_z < 0$, $\omega > 0$.

6. Kink Threshold and Plasma Flow Speed Extracted From Data

6.1. Threshold From PNLT Theory

[42] In Figure 10, data from a series of experiments for three different plasma column lengths ($L = 0.48, 0.92, 1.38$ m) show the scaling of critical current and rotation frequency at criticality, f_{crit} , with the inverse of the column length $1/L$ in agreement with predictions from equations (20) and (21).

[43] The external kink instability in a current rope depends on the magnetic field twist on the “outside surface” of a current channel. For diffuse current profiles such as ours, we must estimate a radial scale length $r = a$. Using the Figure 10 data to constrain I_{crit} , $Re(\omega)$, v_A , L , we can back out $I_{KS} \approx 163 \text{ A} \pm 10\%$ and flow $M \approx 0.25 - 0.4$.

[44] We solve the two equations (20) and (21) by inserting the fitted values for $I_{crit}L$ and $Re(\omega)L$. The two remaining unknown quantities are M and a , from which v_z and I_{KS} can be inferred. Figure 4c reflects this I_{KS} where $I_{crit} \approx 0.45 I_{KS}$.

[45] The experimental parameters for these estimates include a density $n \approx 10^{19} \text{ m}^{-3}$, background magnetic field $B_{z0} = 120 \times 10^{-4}$ Tesla, e.g., from section 2.2 and Figure 2.

[46] From equation (1), the column radius $a \approx 0.02 \pm 10\%$ m. Recall from equation (4) that the flow mach number is referenced to an average Alfvén speed \bar{v}_A that is $\sqrt{2}$ larger than the physical v_A , so the above estimate of $M \approx 0.25 - 0.4$ corresponds to $v_z \approx 3.5 - 6.8 \times 10^4$ m/s. Within the experimental uncertainties this is consistent with the estimates from section 6.2 for $v_z \approx 5 \times 10^4$ m/s at the time during the current ramp when the kink instability threshold is reached.

6.2. Independent Experimental Estimate of Flow

[47] Significant flow exists in our experiment. In RSX the local sound speed decreases along the flux rope path as the local temperature decreases. These RSX flux ropes are therefore locally supersonic because they leave the gun

source region at the local sound speed, and we estimate that the flow speed increases slightly as the rope propagates.

[48] These estimates were carried out by measuring electron density n_e , temperature T_e , and thus the pressure $p = nT$ in $x - y$ cut planes at several z locations. The peak pressure was found to decrease by a factor of two between the plasma gun ($z \approx -0.14$ m and halfway to the external anode axially downstream ($z \approx -0.48$ m). If the flow of the plasma from an RSX gun undergoes gasdynamic acceleration, this process can be described by the expansion of a gas into a vacuum. The axial pressure gradient provides the acceleration.

[49] The ideal MHD equations neglecting magnetic $J \times B$ forces were used where pressure was assumed to be the electron pressure and the mass density was assumed to be the ion mass density. We assumed that flow was mostly in the axial direction, and we solved for the compressible fluid flow profiles. The conclusion was that the plasma flow is initially close the ion acoustic sound speed at the gun nozzle and the speed does not change much downstream. Since the local density, electron temperature, and ion acoustic speed decrease downstream, the flow speed remains approximately. This yields an independent estimate for flow in the range of $v_z \approx 5 \pm 1 \times 10^4$ m/s, which is close to the estimated flow from section 6.1 This estimate is no longer valid once the kink goes unstable and the flux rope becomes helical, because the assumption of one-dimensional behavior breaks down. In the future we will measure the flow directly using electrostatic Mach probes and optical doppler spectroscopy.

7. Chirality and Rotation

7.1. Helical Flux Ropes in the Laboratory

[50] Fast gated optical camera images from previous experiments [Hemsing *et al.*, 2004, 2005] on RSX have shown that flux ropes evolve into helically kinked shapes. The optical emission was also shown to be coincident with maximum current density, electron temperature, and density. Therefore the magnetic and optical measurements presented in this paper correspond to current channels that create paramagnetic perturbations in B_z and differentiate these observations from those expected for drift waves propagating across a low-density background plasma. These conditions are described in the following section 7.

7.2. Kink As Part of the Alfvén Spectrum

[51] In a current carrying plasma, surface Alfvén waves that can be expressed as $\exp(-i\omega t + ik_z z + im\theta)$ and $m \neq 0$ find their symmetry broken with respect to the direction of the background magnetic field. Wave propagation parallel

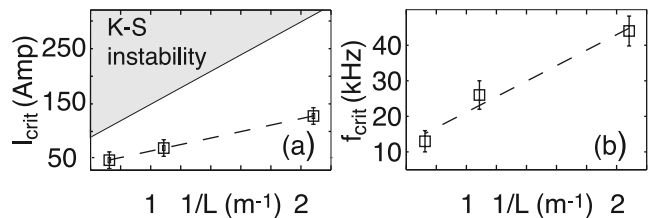


Figure 10. Dependence from $1/L$ of (a) critical current $I_{crit} = 58.8/L$ [A] and (b) rotation frequency at the criticality $f = 2.4 \times 10^4/L$ [Hz].

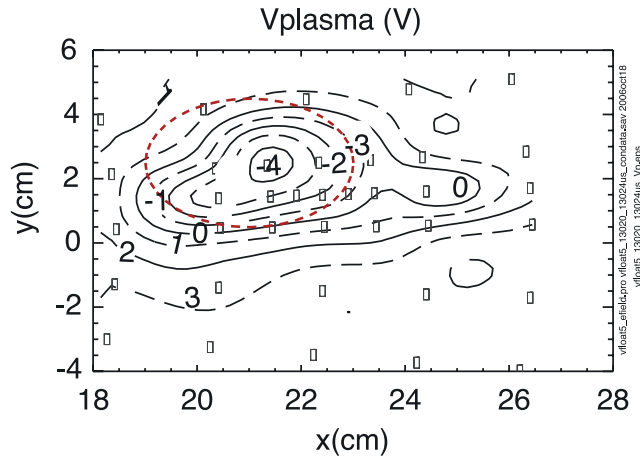


Figure 11. Contours of plasma potential ϕ_p inferred from measurements of floating potential ϕ_f and T_e on the same data grid. An apparent radial electric field $E_r \approx 300\text{--}400\text{ V/m}$ is an order of magnitude greater than would be expected from the kink gyration rotation at $f_{\text{gyr}} \approx 20\text{--}30\text{ kHz}$, a gyration radius of $r_{\text{gyr}} \approx 0.02\text{--}0.03\text{ m}$, and $v_{\text{gyr}} = r_{\text{gyr}} \cdot \omega_{\text{gyr}}$. Flux rope boundary is indicated by a red dashed circle of radius 2 cm (ellipse in this stretched display) centered at $x = 21\text{ cm}$, $y = 2.5\text{ cm}$. Data point positions are indicated by the open squares. Contours alternate solid (even) and dashed (odd) lines.

and antiparallel to the background magnetic field can interact differently with a given field line twist. The kink is an unstable surface Alfvén wave mode with small wave number $k_z c / \omega_{pi} \ll 1$ and $k_z m < 0$. The kink with nominal $k_z > 0$ connects the surface wave dispersion relations [Cramer and Donnelly, 1984; Cross, 1988] between compressional waves at $k_z < 0$ and torsional Alfvén waves at $k_z > 0$.

[52] For the situation described by data in Figure 4 and the sketch of Figure 5 where $k_z > 0$ and $m = -1$, the rotation is in the azimuthal $-\hat{\theta}$ ion diamagnetic drift direction. The experimentally measured rotation of the RSX twisted flux rope is such that it always “screws into” the external anode, or antiparallel to the apparent axial wave number k_z regardless of the background magnetic direction. This is consistent with the theoretical prediction of rotation driven by axial plasma flow directed from the gun to the external anode, as discussed in section 5.

7.3. Ion Diamagnetic Gyration

[53] We have shown data for a kinked RSX flux rope that is a right handed helix with $J_z \cdot B_z > 0$ in Figures 4 and 5. When the axial background magnetic field is reversed with respect to the current such that $J_z \cdot B_z < 0$, we observe a left-handed helix. The experimentally measured handedness of the current rope is consistent with a paramagnetic current channel and kink instability [Hsu and Bellan, 2003].

[54] One simple explanation for the chirality follows from the assumption that kinks involve perturbations with dependence $\exp(-i\omega t + i\mathbf{k} \cdot \mathbf{x})$. It is well known that the instability grows when field line curvature becomes small, i.e., $\mathbf{k} \cdot \mathbf{B} = 0$, so that $k_z = -mB_\theta/(RB_z)$, where R is the radius of (θ) curvature in the $r - \theta$ plane of the gyrating plasma column envelope. For any specified time, a constant phase

$\varphi = \theta - zB_\theta/(RB_z)$ for the kink disturbance results in a pitch $\mathcal{P} = R\theta/z = B_\theta/B_z$. The sign of B_θ/B_z and thus the pitch \mathcal{P} is positive(negative) and right- (left-) handed if $J_z \cdot B_z > 0 (< 0)$.

7.4. Rotation and $\mathbf{E} \times \mathbf{B}$ Drift

[55] It is natural to ask why the rotation is not due to flow but simply due to some electrostatic radial electric field, that induces a $E_r \times B_z$ rotation. This was the mechanism invoked for kink rotation in plasma thruster experiments [Zuin et al., 2004], where they externally applied an electric field.

[56] The theory of Ryutov et al. [2006] and outlined here in section 5 is MHD-like and only invokes sheath electric fields in a general “black box” model at the axial free boundary. Once there is some rotation and hence $v_\theta = r_{\text{gyr}} \cdot \omega_{\text{gyr}}$ in the background magnetic field, we expect some electric field, at least in the tenuous plasma outside the plasma column from Ohm’s Law $\mathbf{E} + \mathbf{v} \times \mathbf{B} = \eta \mathbf{J} + \dots$. If $\eta \mathbf{J}$ is small, one might expect $E_r \approx -v_\theta \times B_z$.

[57] We can estimate radial electric fields by evaluating the local plasma potential ϕ_p . Local electron temperature, density, and floating potential ϕ_f can be measured experimentally using a triple probe. Contours of calculated ϕ_p in the $x - y$ cut plane at $z = -0.48\text{ m}$ from the plasma gun are shown in Figure 11. Data are time-averaged over $4\text{ }\mu\text{sec}$, which is fast enough to “freeze” the motion during the first detectable rotation. For Maxwellian electrons, floating potential is taken to be more negative than the plasma potential $\phi_f \approx \phi_p - 3.5 k_B T_e/e$. The current rope region is indicated by the dashed line ellipse, which we determine from contours (not shown here) of density and current density. The central ϕ_p inside the current rope is negative 3–6 volts from the edge. There results a large radial electric field, on the order of 300–400 V/m, which would yield an $E_r \times B_z$ rotation speed on the order of $3\text{--}4 \times 10^4\text{ m/s}$. One can estimate a “spin” angular frequency $\omega_{\text{spin}} \approx v_E \times B/r_{\text{spin}}$, where $r_{\text{spin}} \approx 1 - 2 \times 10^{-2}\text{ m}$, or a predicted frequency $f_{\text{spin}} = \omega_{\text{spin}}/2\pi \approx 250 - 500\text{ kHz}$. This rotation speed is an order of magnitude larger than any reasonable estimate of the gyration speed v_θ , and in the opposite $+\hat{\theta}$ electron diamagnetic direction. However, f_{spin} is not too far from the expected drift Alfvén rotation frequency, as we will see next in section 8. We conclude that the kink gyration that we attribute to the effects of axial flow could not be caused by this $\mathbf{E} \times \mathbf{B}$ rotation. An inductive electric field due to a Hall type $\mathbf{v} \times \mathbf{B}$ effect might not be straightforward to interpret by using electrostatic probe data. In any case the appropriate electric field would have to be divergence-free in the volume of interest.

[58] The local plasma potential in any volume of interest is dependent on some balance of charge inflow and outflow. Both could be due to parallel and perpendicular current densities and diffusion, which could lead to either a local potential minimum or maximum, depending on the details. For an electrostatic problem with Maxwellian electrons and immobile ions one might expect a local positive potential in the current channel center which we do not observe in Figure 11.

8. Kink Versus Drift Alfvén Wave

[59] The global, helical kink we that we measure has substantially different characteristics from the local drift

Alfvén wave. In order to illustrate the distinction, we contrast some properties of the drift Alfvén wave with those of the kink.

[60] When the Alfvén and electron diamagnetic drift speed approach each other, drift waves and Alfvén waves form a coupled spectrum. The drift wave is an internal mode, with density and magnetic field fluctuations localized near the maximum pressure gradient or if the temperature does vary too much, near the maximum density gradient [Tang *et al.*, 1975; Tang and Luhman, 1976]. Axial current is required to drive the drift wave instability, which for positive $k_z > 0$ is in the $+\hat{\theta}$ electron diamagnetic drift direction, the frequency range is similar, and there is a finite axial wave length of the order of the device length. When the magnetic field produced by electron axial oscillation in the drift wave is taken into account, one obtains a drift-Alfvén wave with rotating magnetic oscillations. It is possible that the global kink perturbations also existed in Tang's [Tang and Luhman, 1976] experiment. Their threshold for the Alfvén branch of the drift-Alfvén spectrum is suspiciously close to the KS limit for the internal kink. Drift waves with small magnetic oscillations were reported [Kauschke, 1992] in a linear device with some parameters similar to RSX.

[61] The kink mode contrasts with the drift wave which for $k_z > 0$ propagates in the electron diamagnetic $+\hat{\theta}$ direction at rotation frequency

$$\omega_{De} = \frac{\omega^*}{1 + k_\perp^2 \rho_s^2} \quad (22)$$

$$\omega^* = v_{De}/a = \frac{T_e}{eBL_p r_{spin}} \quad (23)$$

where $L_p \approx 0.02$ m is the radial pressure scale length, $r_{spin} \approx 0.01$ m is the flux rope "spin" radius, $v_{De} \approx 2 \times 10^4$ m/s is the electron drift speed. Finite larmor radius ρ_s effects are expressed in terms of a perpendicular wave number k_\perp correction where the fastest growth rate occurs for $k_\perp \rho_s \approx 1$. For typical RSX parameters $T_e \approx 10$ eV, $\rho_s \approx 1 - 2 \times 10^{-2}$ m, so that for the $m = +1$ mode,

$$f_{De} \approx 250 \text{ kHz} \quad (24)$$

is the opposite direction and an order of magnitude larger than our observed rotation frequency (see, e.g., Figure 10) of $f_{rot} \approx 20\text{--}40$ kHz.

[62] A true kink will gyrate to paramagnetically amplify the zero-order B_z as we discuss in section 7, whereas a drift-wave will spin the plasma moving across a background magnetic field without altering the field to lowest order. The measured paramagnetic property distinguishes the RSX kink from the expected behavior of the drift Alfvén wave. The arguments about axial boundary conditions (line-tied versus not line-tied) could be equally made for a drift wave as for a kink. The saturated nature of the oscillation that we point out here is a known feature of drift waves but has not been explored for kinks.

9. Discussion

9.1. Key Results

[63] We have experimentally shown for the first time that a paramagnetic kink instability can occur in a plasma

current rope with one free foot point that is not line tied to its boundary. The axial eigenfunction shape shown in Figure 8 resembles a one quarter wavelength structure, displacement is large at the free end, and it goes unstable at a critical threshold substantially lower than the Kruskal-Shafranov limit. Indeed, the quarter wavelength would be an exact description if the axial boundary condition $\partial\zeta/\partial z|_{z=L} = 0$ had been invoked in place of equation (6). The typically observed but never explained nonzero rotation instability frequency [Zuin *et al.*, 2004] is likely due to a Doppler shift from the plasma flow and finite axial wave number.

[64] It is not clear how much these details affect the long-lifetime saturated states, for example the one we show in Figure 4b. The experimental examples shown in this paper persist as long as the flux rope is sustained by the gun (several msec), which is much longer than the μ s Alfvén timescale. Long-lifetime kink-like states have been observed in other experiments where PNLT likely applies [Zuin *et al.*, 2004] and without PNLT [Bergerson *et al.*, 2006] boundary conditions.

[65] The phenomenological kink theory [Ryutov *et al.*, 2006] predicts as a consequence of flow: (1) Flow-driven rotation frequency depending on column length. (2) A rotation sense in the ion diamagnetic direction for $k_z > 0$, so that the kink screws in the $-k_z$ direction into the external anode. (3) Gyration eigenfunction shape whose radius increases as it is advected in the flow direction. (4) Increased instability drive from centripetal force as the flow follows curved streamlines. We have discussed the properties of the drift Alfvén wave and shown that it cannot account for our experimental observations.

[66] It is curious that the ion diamagnetic kink gyration and the inferred electron diamagnetic spin of the column are in opposite directions. It is likely that the spin rotates an order of magnitude faster than the gyration. The moment of inertia for the spin is estimated to be an order of magnitude less than the moment of inertia for the gyration. Perhaps total angular momentum is conserved.

9.2. Force Balance

[67] The force balance for the flux rope with one free end has some important differences from the usual case with two fixed ends. For relaxing helical currents, there is a destabilizing $J_\theta \times B_z$ force density giving rise to the force density ∇B^2 that coexists with a stabilizing restoring force density proportional to field line curvature and $\vec{B} \cdot \nabla \vec{B}$. The external kink mode grows when the restoring force vanishes. The free end of the kinking column allows end displacement but with reduced curvature and restoring force compared to what is expected with a constrained end. Once the flux rope is gyrating, flow along the curved field lines results in a centripetal force that tends to drive the kink even more unstable. This is consistent with our experimentally observed stability threshold that is reduced to less than one half of the usual Kruskal-Shafranov predictions.

9.3. Relevance to Natural and Laboratory Plasmas

[68] Some of the physics relevant to the MHD-like behavior of open flux tubes in nature and the laboratory corresponds to the RSX non-line-tied boundary condition at one end. These experimental conclusions about the dynamics of the kink could be important for the MHD evolution

and relaxation of plasmas in nature. For instance, the kink threshold for PNLT flux ropes is less than half of the usual estimate. Moreover, if there is sufficient flow, equations (16) for PLT and equations (17) and (20) for PNLT show that the kink threshold can be very low indeed. This could elicit the onset of kink instability even in situations where the inferred magnetic twist is small enough that the possibility of kink deformations has not previously been considered.

[69] Magnetic flux and particles escaping from the solar corona have several features in common with our experimental flux ropes. Open magnetic flux originates at coronal holes [Axford et al., 1999; Krieger et al., 1973], which source the fast solar wind. This represents a significant portion of the solar wind. After solar eruptions, magnetic flux structures and particle trajectories can also open up to the magnetosphere, for example in the formation of magnetic clouds. Significant flow exists in our experiment, which is also a feature of the flow of solar wind particles that leave the Sun. Flow has been inferred in preeruption solar flux ropes [Krall and Chen, 2005]. In the solar wind case there is a transition from subsonic and sub-Alfvénic to supersonic and super-Alfvénic flow. In RSX, the flow transitions to supersonic far from the plasma gun.

[70] In astrophysical jets, there clearly is one end anchored at the accretion disc source region. The other end is very far away, and if there is significant magnetic field and current, these may engender open flux structures and magnetic field lines that are very long, either with respect to the correlation collision length or Alfvén wave transit time. One interesting example [Morris et al., 2006] is an infrared image of double helix jet-like helical structures emanating from the galactic plane Milky Way disc. These helices are quite large and persistent, and have been identified as the signature of an torsional Alfvén wave. Viewed from far away, other astrophysical jets can display apparently kinked shapes that have previously been explained as soliton structures [Lapenta, 2003] and resemble RSX images [Hemming et al., 2005]. In practical devices, magnetoplasma dynamic thrusters for space propulsion applications involve magnetic field lines that terminate on the spacecraft or thruster itself.

[71] The kink mode is the simplest 3-D deformation of a current carrying MHD system. During the last 50 years, much has been learned about the kink, but little has been reported about the effect of axial boundary conditions. Most theoretical approaches are either toroidal or axially periodic. We have argued here that there are interesting natural and laboratory plasmas that are subject to non-line-tied axial boundary conditions. Experimental data shown here show remarkable agreement with a theoretical picture [Ryutov et al., 2006] that includes incident and reflected Alfvén waves on the surface of the flux rope.

[72] **Acknowledgments.** The authors are grateful for support by Los Alamos Laboratory Directed Research and Development-Exploratory Research program and Department of Energy contract DE-AC52-06NA25396.

[73] Amitava Bhattacharjee thanks the reviewers for their assistance in evaluating this paper.

References

- Axford, W. I., J. F. McKenzie, G. V. Sukhorukova, M. Banaszkiewicz, A. Czechowski, and R. Ratkiewicz (1999), Acceleration of the high speed solar wind in coronal holes, *Space Sci. Rev.*, 87(1-2), 25–41.
- Benford, G. (1997), The electrodynamic ‘snake’ at the galactic centre, *Mon. Not. R. Astron. Soc.*, 285(3), 573–579.
- Bergerson, W. F., C. B. Forest, G. Fiksel, D. A. Hannum, R. Kendrick, J. S. Sarff, and S. Stambler (2006), Onset and saturation of the kink instability in a current-carrying line-tied plasma, *Phys. Rev. Lett.*, 96, 015004.
- Berk, H. L., D. D. Ryutov, and Y. A. Tsidulko (1990), Temperature gradient instability caused in plasma by conducting end surfaces, *JETP Lett.*, 52(1), 23.
- Cramer, N., and I. Donnelly (1984), Surface and discrete alfvén waves in a current carrying plasma, *Plasma Phys. Control. Fusion*, 26(11), 1285–1298.
- Cross, R. (1988), *An Introduction to Alfvén Waves*, The Adam Hilger Ser. on Plasma Phys., IOP Publ., Philadelphia, Penn.
- Fiksel, G., A. Almagri, D. Craig, M. Iida, S. Prager, and J. Sarff (1996), High current plasma electron emitter, *Plasma Sources Sci. Technol.*, 5, 78–83.
- Furno, I., T. Intrator, E. Torbert, C. Carey, M. D. Cash, J. K. Campbell, W. J. Fienup, C. A. Werley, G. A. Wurden, and G. Fiksel (2003), Reconnection scaling experiment: A new device for three-dimensional magnetic reconnection studies, *Rev. Sci. Instrum.*, 74(4), 2324.
- Furno, I., T. P. Intrator, D. Ryutov, S. Abbate, T. Madziwa-Nussinov, A. Light, L. Dorf, and G. Lapenta (2006), Current-driven rotating-kink mode in a plasma column with a non-line-tied free end, *Phys. Rev. Lett.*, 97, 015,002.
- Hegna, C. C. (2004), Stabilization of line tied resistive wall kink modes with rotating walls, *Phys. Plasmas*, 11(9), 4230.
- Hemming, E., I. Furno, T. Intrator, and D. Wei (2004), Analysis of visible light images from a fast-gated intensified ccd camera during flux rope interaction and magnetic reconnection, *Rev. Sci. Instrum.*, 75(10), 4106–4108.
- Hemming, E., I. Furno, and T. Intrator (2005), Fast camera images of flux ropes during plasma relaxation, *IEEE Trans. Plasma Sci.*, 33(2), 448–449.
- Hsu, S. C., and P. M. Bellan (2003), Experimental identification of the kink instability as a poloidal flux amplification mechanism for coaxial gun spheromak formation, *Phys. Rev. Lett.*, 90(21), 215,002.
- Kadomtsev, B. (1966), Hydromagnetic stability of a plasma, *Rev. Plasma Phys.*, 2, 153.
- Kauschke, U. (1992), On the influence of magnetic fluctuations on the electrostatic spectrum of a magnetized plasma column, *Plasma Phys. Control. Fusion*, 34(7), 1303.
- Krall, J., and J. Chen (2005), Density structure of a preeruption coronal flux rope, *Astrophys. J.*, 628(2), 1046.
- Krieger, A. S., A. F. Timothy, and E. C. Roelof (1973), A coronal hole and its identification as the source of a high velocity solar wind stream, *Solar Phys.*, 29(2), 505–525.
- Kruskal, M., and J. L. Tuck (1958), The instability of a pinched fluid with a longitudinal magnetic field, *Proc. R. Soc. London, Ser. A*, 245(1241), 222–237.
- Kumar, A., and D. Rust (1996), Interplanetary magnetic clouds, helicity conservation and intrinsic-scale flux ropes, *J. Geophys. Res.*, 101, 15,667.
- Lanskii, I. M., and A. I. Shchetnikov (1990), Kink instability of plasma column with frozen-in ends, *Sov. J. Plasma Phys.*, 16, 322.
- Lapenta, G. (2003), Soliton-like solutions of the grad-shafranov equation, *Phys. Rev. Lett.*, 90, 135,005.
- Li, H., R. V. E. Lovelace, J. M. Finn, and S. A. Colgate (2001), Magnetic helix formation driven by keplerian disk rotation in an external plasma pressure: the initial expansion stage, *Astrophys. J.*, 561(2), 915.
- Lovelace, R. V. E. (1976), Dynamo model of double radio sources, *Nature*, 262(5570), 649.
- Morris, M., K. Uchida, and T. Do (2006), A magnetic torsional wave near the galactic centre traced by a “double helix” nebula, *Nature*, 440, 308.
- Rust, D. M., and B. J. LaBonte (2005), Observational evidence of the kink instability in solar filament eruptions and sigmoids, *Astrophys. J.*, 622(1), L69.
- Ryutov, D. D., R. H. Cohen, and L. D. Pearlstein (2004), Stability of a finite-length screw pinch revisited, *Phys. Plasmas*, 11(10), 4740.
- Ryutov, D. D., I. Furno, T. P. Intrator, S. Abbate, and T. Madziwa-Nussinov (2006), Phenomenological theory of the kink instability in a slender plasma column, *Phys. Plasmas*, 13(3), 032,105.
- Sakurai, T. (1976), Magnetohydrodynamic interpretation of the motion of prominences, *Publ. Astron. Soc. Jpn.*, 28(2), 177.
- Schrijver, C., and Z. Cornelis (2000), *Solar and Stellar Magnetic Activity*, Cambridge Univ. Press, New York.
- Shafranov, V. (1956), On the stability of a cylindrical gaseous conductor in a magnetic field, *Atomic Energy*, 5, 38.
- Sovinec, C. R., J. M. Finn, and D. del Castillo-Negrete (2001), Formation and sustainment of electrostatically driven spheromaks in the resistive magnetohydrodynamic model, *Phys. Plasmas*, 8, 475–490.

- Tang, J., and N. Luhman (1976), Destabilization of hydromagnetic drift-Alfvén waves in a finite pressure, collisional plasma, *Phys. Fluids*, 19(12), 1935–1946.
- Tang, J., N. Luhman, Y. Nishida, and I. Kazushige (1975), Destabilization of hydromagnetic drift waves in a finite beta collisional plasma, *Phys. Rev. Lett.*, 34(2), 70–73.
- Verhage, A. J. L., A. S. Furzer, and D. C. Robinson (1978), Observations of large-amplitude helical kink instabilities and field reversal in a fast pinch experiment (hbt-x-1), *Nucl. Fusion*, 18(4), 73–457.
- Zuin, M., R. Cavazzana, E. Martines, G. Serianni, V. Antoni, M. Bagatin, M. Andreucci, F. Paganucci, and P. Rossetti (2004), Kink instability in applied-field magneto-plasma-dynamic thrusters, *Phys. Rev. Lett.*, 92(22), 225,003.
- Zweibel, E. G., and A. H. Boozer (1985), Evolution of twisted magnetic fields, *Astrophys. J.*, 295(2), 642–647.
-
- L. Dorf, I. Furno, T. P. Intrator, and X. Sun, Los Alamos National Laboratory, M.S. E526, Los Alamos, NM 87545, USA. (intrator@lanl.gov)
- G. Lapenta, Plasma Theory, Los Alamos National Laboratory, Los Alamos, NM 87545, USA.
- D. D. Ryutov, Lawrence Livermore National Laboratory, Livermore, CA 94551, USA.